

# Kernel Descent – a Novel Optimizer for Variational Quantum Algorithms

Lars Simon<sup>\*</sup>, Holger Eble<sup>†</sup>, and Manuel Radons<sup>‡</sup>

*Bundesdruckerei GmbH, Kommandantenstraße 18, 10969 Berlin, Germany*

## Abstract

In recent years, variational quantum algorithms have garnered significant attention as a candidate approach for near-term quantum advantage using noisy intermediate-scale quantum (NISQ) devices. In this article we introduce kernel descent, a novel algorithm for minimizing the functions underlying variational quantum algorithms. We compare kernel descent to existing methods and carry out extensive experiments to demonstrate its effectiveness. In particular, we showcase scenarios in which kernel descent outperforms gradient descent and quantum analytic descent. The algorithm follows the well-established scheme of iteratively computing classical local approximations to the objective function and subsequently executing several classical optimization steps with respect to the former. Kernel descent sets itself apart with its employment of reproducing kernel Hilbert space techniques in the construction of the local approximations – which leads to the observed advantages.

## 1 INTRODUCTION

The promise of exponential computational advantages from quantum computing remains unrealized in practice due to the noisiness and limited qubit count of currently available quantum hardware. Variational quantum algorithms (VQAs) have risen to prominence as a promising strategy to achieve utility of quantum computers in the near term, within the constraints of the so-called noisy intermediate-scale quantum (NISQ) era.

VQAs leverage a classical optimizer to train a parametrized quantum circuit, drawing parallels to classical machine learning models such as neural networks [CAB<sup>+</sup>21]. The primary objective of VQA training, in its most basic form, is to find a choice of parameters for a parametrized quantum circuit that minimizes the expected value of a given observable with respect to the state computed by the circuit. This adaptive approach, combined with the typically shallower circuit depths required compared to algorithms designed for fault-tolerant quantum computing, accounts for the expected NISQability of the approach [CAB<sup>+</sup>21].

A common strategy for the minimization of the objective function underlying a VQA involves computing a local approximation around a given point in parameter space, followed by one or more classical optimization steps with respect to this approximation. The outcome of this procedure yields the next base point for a local approximation of the function and the process is repeated until a predefined convergence criterion is met. Arguably, the most prominent representatives of this training philosophy are gradient descent (via linear approximations), and quantum analytic descent (via trigonometric approximations). There also exist derivative-free methods—for example, Nelder-Mead [NM65], Powell [Pow64], COBYLA [Pow94]—as well as methods designed specifically for the functions underlying VQAs, such as Rotosolve [OGB21], [VT18],

[NFT20], [PIOM19]. However, gradient-based optimizers are more common in the context of VQAs. The evaluations of the gradients are usually performed via the parameter-shift rules, even though the required number of circuit evaluations scales unfavorably with the number of trainable parameters, cf. [BWP23], [AKH<sup>+</sup>23]. For information on parameter-shift rules, see [MNKF18], [SBG<sup>+</sup>19], [MBK21], [WIWL22].

In this article, we introduce kernel descent, a novel training algorithm for VQAs. Kernel descent follows the iterative optimization process described above. Its key innovation is the exploitation of the fact that the functions computed by VQAs are contained in a set which naturally carries the structure of a reproducing kernel Hilbert space (RKHS). This approach often leads to an improved quality of the local approximations computed during training, to which we ascribe the algorithm’s observed performance advantages, particularly in terms of speed of convergence and robustness. We note that neither measurement shot noise nor quantum hardware noise are taken into account in the theoretical description of kernel descent. However, in [SEKR24a] we demonstrated experimentally that our RKHS techniques can in fact be used to mitigate the adverse effects of both these types of noise.

Kernel descent introduces a hyperparameter  $L$  that governs the order of the local approximations computed during its execution. As  $L$  increases, the approximation quality improves, albeit with a corresponding increase in the number of circuit evaluations per iteration. For  $L = 1$ , the number of circuit evaluations per iteration is comparable to that of gradient descent using the parameter-shift rules, and for  $L = 2$ , it is comparable to that of quantum analytic descent. Consequently, our experiments will compare the performance of kernel descent with  $L = 1$  and  $L = 2$  to that of gradient descent and quantum analytic descent, respectively.

To level the playing field, all algorithms will be tested

<sup>\*</sup>lars.simon@bdr.de

<sup>†</sup>holger.eble@bdr.de

<sup>‡</sup>manuel.radons@bdr.de

in their most basic form, without adaptive learning rates or similar enhancements. Advanced techniques, such as normalized gradient descent [HLSS15], Nesterov’s Accelerated Gradient method [Nes83], the ADAM optimizer [KB15], or natural gradient descent [Ama98], can be adapted to kernel descent (see [SYRY21] and [SIKC20] for their treatment in the context of VQAs). However, we leave this task for future investigations as it would go beyond the scope of this work.

The present article is part of a larger study on the use of RKHS techniques in the context of VQAs. This approach has already been employed in constructing classical surrogates of quantum machine learning models [SEKR24b] and, as mentioned above, in alleviating the adverse effects of noise on gradient descent in VQAs [SEKR24a]. The project originated in the application of RKHS methods to the training of neural support vector machines [SR23a], which subsequently led to the development and analysis of neural quantum support vector machines in [SR23b]. This series of investigations laid the groundwork for the development of kernel descent as a robust optimization strategy specifically tailored to the functions underlying VQAs.

**Content and Structure:** In Section 2, after laying out our assumptions and the optimization task, we introduce kernel descent and provide a detailed comparison of the algorithm’s underlying theory with that of gradient descent and quantum analytic descent. Building on this groundwork, Section 3 presents the results of our experimental comparison of kernel descent to gradient descent and quantum analytic descent, providing empirical evidence for the claimed advantages in terms of speed of convergence and, particularly, robustness of the novel algorithm. Our closing remarks, including a discussion of the results and suggestions for future research directions, follow in Section 4.

## 2 ALGORITHM

In Section 2.1 we establish the setting and state the problem addressed by our algorithm; subsequently, in Section 2.2, we go over some technical preliminaries. In Section 2.3 we state the general strategy used to tackle the problem, before giving a detailed description of our algorithm, including performance guarantees, in Section 2.4. Finally, in Section 2.5, we compare our algorithm to gradient descent and quantum analytic descent.

### 2.1 Setting

Letting  $m, n \in \mathbb{Z}_{>0}$ , we consider functions of the form  $f: \mathbb{R}^m \rightarrow \mathbb{R}$ ,

$$f(\theta) = \langle \psi(\theta) | \mathcal{M} | \psi(\theta) \rangle, \quad (1)$$

where  $\mathcal{M} \in \mathbb{C}^{2^n \times 2^n}$  is an observable and

$$|\psi(\theta)\rangle = C_{m+1} R_m(\theta_m) C_m \cdots R_1(\theta_1) C_1 |0\rangle^{\otimes n},$$

where  $C_1, \dots, C_{m+1}$  are  $n$ -qubit unitaries and, for all  $j \in \{1, \dots, m\}$ ,

$$R_j(\theta_j) = \exp\left(-i \frac{\theta_j}{2} G_j\right), \theta_j \in \mathbb{R},$$

is a rotation, where  $G_j \in \mathbb{C}^{2^n \times 2^n}$  is Hermitian with set of eigenvalues  $\{-1, 1\}$  (e.g.,  $G_j$  could be an element of  $\{I, X, Y, Z\}^{\otimes n} \setminus \{I^{\otimes n}\}$ , where  $I, X, Y, Z$  denote the Pauli matrices). For a visual representation of the corresponding circuits, see Figure 1.

The goal is now to minimize the function  $f$ , i.e., to find a point in parameter space  $\mathbb{R}^m$ , at which the value of  $f$  is minimal. The most commonly-used algorithm for this task is gradient descent using the parameter-shift rules [MNKF18], [SBG<sup>+</sup>19], [MBK21], [WIWL22], which requires  $2m$  circuit evaluations per iteration. Another algorithm is quantum analytic descent [KB22], which requires  $2m^2 + m + 1$  circuit evaluations per iteration. Both of these, as well as the algorithm we will introduce in Section 2.4, are a special case of the technique introduced in Section 2.3.

### 2.2 Technical preliminaries

It follows from the results in [SSM21] that  $f$  (see Section 2.1) is contained in  $H$ , where  $H$  is the set of all functions  $g: \mathbb{R}^m \rightarrow \mathbb{R}$  of the form  $g(z) = \sum_{\omega \in \{-1, 0, 1\}^m} c_\omega e^{i\omega^\top z}$  with  $\overline{c_{-\omega}} = c_\omega \in \mathbb{C}$  for all  $\omega \in \{-1, 0, 1\}^m$ . When equipping  $H$  with the (real) inner product given by

$$\langle g_1, g_2 \rangle_H = \int_{[-\pi, \pi]^m} g_1(z) g_2(z) dz, \quad g_1, g_2 \in H,$$

it turns out that  $H$  carries the structure of a reproducing kernel Hilbert space with kernel  $K = \left(\frac{3}{2\pi}\right)^m \tilde{K}$ , where

$$\tilde{K}(x, z) = \prod_{j=1}^m \frac{1 + 2 \cos(x_j - z_j)}{3}, \quad x, z \in \mathbb{R}^m.$$

The following lemma shows how the structure of  $H$  can be exploited to obtain approximations of  $f$ :

**Lemma 1.** *Let  $D \in \mathbb{Z}_{\geq 1}$  and let  $p_1, \dots, p_D \in \mathbb{R}^m$ . Then the linear system of equations*

$$\left(\tilde{K}(p_i, p_j)\right)_{1 \leq i, j \leq D} \cdot \tilde{\eta} = (f(p_1), \dots, f(p_D))^\top$$

*has at least one solution  $\tilde{\eta} \in \mathbb{R}^D$ , allowing us to define  $\tilde{f}: \mathbb{R}^m \rightarrow \mathbb{R}$  given by*

$$\tilde{f}(\theta) = \sum_{j=1}^D \tilde{\eta}_j \tilde{K}(p_j, \theta).$$

*We then have:*

- $\tilde{f}$  does not depend on the choice of (the not necessarily uniquely determined)  $\tilde{\eta}$ .
- $\tilde{f}$  is the orthogonal projection (wrt.  $\langle \cdot, \cdot \rangle_H$ ) of  $f$  onto the subspace of  $H$  spanned by  $K(p_1, \cdot), \dots, K(p_D, \cdot)$ .
- $\tilde{f}(p_j) = f(p_j)$  for  $j = 1, \dots, D$ .

*Proof.* This is obvious from the results in [SEKR24b], specifically Implementation Remark 6 and Lemma 13.  $\square$

In order to compute the approximation given by Lemma 1, we need to solve a linear system of equations. However, for specific choices of the points  $p_1, \dots, p_D$ , the occurring matrix becomes trivial to invert. One such choice is given by the following lemma:

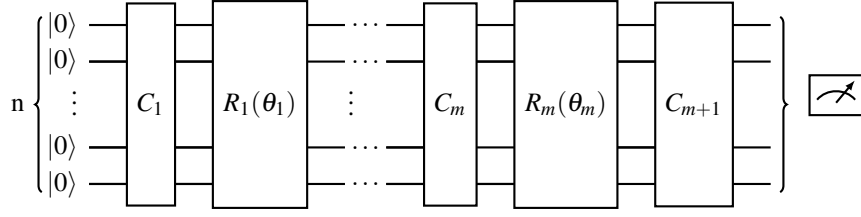


Figure 1: This figure shows the circuit underlying the computation of the function  $f$  in Section 2.1.

**Lemma 2.** For all  $p \in \mathbb{R}^m$ , the family

$$\left( \sqrt{\left(\frac{2\pi}{3}\right)^m} K(p+q, \cdot) \right)_{q \in \left\{-\frac{2\pi}{3}, 0, \frac{2\pi}{3}\right\}^m}$$

is an orthonormal basis for  $H$ .

*Proof.* Since  $\dim_{\mathbb{R}}(H) = 3^m = \text{card}\left(\left\{-\frac{2\pi}{3}, 0, \frac{2\pi}{3}\right\}^m\right)$ , the claim follows from explicitly calculating the pairwise inner products of the members of the given family.  $\square$

### 2.3 Strategy

When aiming to minimize  $f$ , a common technique is to compute a local approximation around a given point in parameter space  $\mathbb{R}^m$  and subsequently perform one (or several) optimization step(s) with respect to this approximation. More precisely, the technique consists of the following steps:

1. Pick an initial point  $\theta_0 \in \mathbb{R}^m$  in parameter space.
2. For  $t = 0, 1, \dots, T-1$ :
  - (a) Compute a classical local approximation  $\tilde{f}_t$  of  $f$  around  $\theta_t$  (this typically involves the execution of various quantum circuits).
  - (b) Execute one (or several) classical optimization step(s) with respect to  $\tilde{f}_t$  and obtain a point  $\theta_{t+1} \in \mathbb{R}^m$  in parameter space.
3. Output  $\theta_T$ .

Instead of executing a fixed number of iterations  $T$ , one can, of course, impose some other stopping criterion. We remark that gradient descent can be seen as a special case of this technique, since computing the value of the function and its gradient at a point in parameter space is equivalent to computing the best local linear approximation at this point. Likewise, quantum analytic descent is a special case of this technique: The local approximation computed during quantum analytic descent is a trigonometric polynomial that coincides with  $f$  up to second order at the given point in parameter space.

The algorithm we will present in Section 2.4 also follows the above recipe; in light of this, we only need to describe how to obtain local approximations of  $f$  around points in parameter space.

### 2.4 Description of the algorithm

Our algorithm employs the technique introduced in Section 2.3. Accordingly, it suffices to describe how we construct local approximations of  $f$  around points in parameter space. To this end, let  $p \in \mathbb{R}^m$  be a fixed point in parameter space. We introduce a hyperparameter  $L \in \mathbb{Z}$ , where  $1 \leq L \leq m$ , which controls the order of the approximation. We then determine all points  $q_1, \dots, q_D \in \left\{-\frac{2\pi}{3}, 0, \frac{2\pi}{3}\right\}^m$  with the property that at most  $L$  entries are non-zero (without repetitions, i.e.,  $q_i \neq q_j$  whenever  $i \neq j$ ). Now, for  $j = 1, \dots, D$ , we set  $p_j := p + q_j \in \mathbb{R}^m$ . Following Lemma 1, we then obtain an approximation  $\tilde{f}: \mathbb{R}^m \rightarrow \mathbb{R}$  to  $f$  by setting  $\tilde{f}(\theta) = \sum_{j=1}^D \tilde{\eta}_j \tilde{K}(p_j, \theta)$ , where  $\tilde{\eta} \in \mathbb{R}^D$  is a solution to the linear system of equations

$$\left(\tilde{K}(p_i, p_j)\right)_{1 \leq i, j \leq D} \cdot \tilde{\eta} = (f(p_1), \dots, f(p_D))^{\top}.$$

At first glance it seems like the need to solve this linear system of equations entails a large classical computational overhead. However, the points  $p_1, \dots, p_D$  were specifically chosen so that the occurring matrix is the identity matrix, see Lemma 2. It follows that  $\tilde{\eta} = (f(p_1), \dots, f(p_D))^{\top}$ , so that  $\tilde{f}: \mathbb{R}^m \rightarrow \mathbb{R}$  is given by

$$\tilde{f}(\theta) = \sum_{j=1}^D f(p_j) \tilde{K}(p_j, \theta) = \sum_{j=1}^D f(p+q_j) \tilde{K}(q_j, \theta-p). \quad (2)$$

In order to obtain this approximation  $\tilde{f}$ , we need a quantum device to evaluate  $f$  in  $p+q_1, \dots, p+q_D$ . Note that due to the exact formula (2) this approach entails no classical computational overhead. The following result guarantees that  $\tilde{f}$  is indeed a good local approximation of  $f$  around  $p$ .

**Theorem 3.** Let  $p \in \mathbb{R}^m$ , and let  $L \leq m$  be a positive integer. Moreover, let  $q_1, \dots, q_D$  be the pairwise distinct elements of  $\left\{-\frac{2\pi}{3}, 0, \frac{2\pi}{3}\right\}^m$  with the property that at most  $L$  entries are non-zero. Now, define  $\tilde{f}: \mathbb{R}^m \rightarrow \mathbb{R}$  by

$$\tilde{f}(\theta) = \sum_{j=1}^D f(p+q_j) \tilde{K}(q_j, \theta-p) \text{ for all } \theta \in \mathbb{R}^m.$$

Then the following holds:

- (i) In order to obtain the approximation  $\tilde{f}$ , one needs to evaluate  $f$  in  $D = \sum_{k=0}^L 2^k \cdot \binom{m}{k}$  points in parameter space.
- (ii) If  $\vartheta \in \mathbb{R}^m$  has at most  $L$  non-zero entries, then  $\tilde{f}(p+\vartheta) = f(p+\vartheta)$ . That is,  $\vartheta \mapsto \tilde{f}(p+\vartheta)$  coincides with  $\vartheta \mapsto f(p+\vartheta)$  on any subspace of  $\mathbb{R}^m$  that is spanned by at most  $L$  of the coordinate axes.

(iii)  $\tilde{f}$  coincides with  $f$  up to order  $L$  locally around  $p$ .  
More precisely, we have  $D^\alpha(f - \tilde{f})(p) = 0$  for all multiindices  $\alpha \in (\mathbb{Z}_{\geq 0})^m$  with  $|\alpha| \leq L$ .

*Proof.* This follows analogously to the proof of Theorem 7 in [SEKR24b].  $\square$

A compact description of our algorithm in pseudocode, bringing together the technique outlined in Section 2.3 with the specific choice of local approximation described in Section 2.4, can be found in Algorithm 1.

---

**Algorithm 1: Kernel Descent**

---

**Input** : order  $L$ , number of iterations  $T \in \mathbb{Z}_{\geq 1}$ ,  
function  $f: \mathbb{R}^m \rightarrow \mathbb{R}$ ,  
 $f(\theta) = \langle \psi(\theta) | \mathcal{M} | \psi(\theta) \rangle$  (see Section 2.1)

**Output:** point  $\theta_T \in \mathbb{R}^m$  in parameter space

- 1 Determine the pairwise distinct elements  $q_1, \dots, q_D$  of  $\{-\frac{2\pi}{3}, 0, \frac{2\pi}{3}\}^m$  with the property that at most  $L$  entries are non-zero
- 2 Pick an initial point  $\theta_0 \in \mathbb{R}^m$  in parameter space  
**for**  $t = 0, 1, \dots, T - 1$  **do**
- 3 **for**  $j = 1, 2, \dots, D$  **do**  
Evaluate  $f(\theta_t + q_j)$  using a quantum device  
**end**
- 4 Set  $\tilde{f}_t(\theta) = \sum_{j=1}^D f(\theta_t + q_j) \tilde{K}(q_j, \theta - \theta_t)$
- 5 Execute one (or several) classical optimization step(s) with respect to  $\tilde{f}_t$  and obtain a point  $\theta_{t+1} \in \mathbb{R}^m$  in parameter space  
**end**
- 6 **return**  $\theta_T$

---

In Algorithm 1, the method for minimizing the classical approximations  $\tilde{f}_t$  is intentionally left open in order to not limit the generality of the algorithm. A natural approach would be to carry out several gradient descent steps with respect to  $\tilde{f}_t$ , whose gradient can be computed efficiently.

## 2.5 Comparison with existing approaches

Since all algorithms investigated below are based on computing and subsequently optimizing local approximations (see also Section 2.3) we limit ourselves to comparing the quality of the latter. It follows from Theorem 3(i) that the number of evaluations of  $f$  needed by Algorithm 1 to compute the local approximation  $\tilde{f}_t$  does not exceed (but is comparable to) the number of evaluations necessary to compute the  $L$ -th order Taylor polynomial about  $\theta_t$  using the parameter-shift rules for arbitrary-order partial derivatives [MBK21], [WIWL22], [SEKR24b]. Moreover, Theorem 3(iii) guarantees that  $\tilde{f}_t$  coincides with  $f$  up to order  $L$  locally around  $\theta_t$ , and the same holds true for the  $L$ -th order Taylor polynomial about  $\theta_t$ . However, in contrast to the  $L$ -th order Taylor polynomial about  $\theta_t$ , the *local* approximation  $\tilde{f}_t$  is guaranteed to preserve some *global* properties of  $f$ , such as the periodicity of  $f$  (since  $\tilde{f}_t \in H$ ) and the values of  $f$  along certain  $L$ -dimensional affine subspaces through  $\theta_t$  (by Theorem 3(ii)). A heuristic explanation for these advantages is that Algorithm 1 exploits the intrinsic structure of  $H$ , which is a finite-dimensional subspace of the much

larger infinite-dimensional space of smooth  $\mathbb{R}$ -valued functions on  $\mathbb{R}^m$ , to which Taylor approximations generically apply. In the experiments in [SEKR24b] the approximations featuring in Algorithm 1, albeit with  $\pm \frac{\pi}{2}$  parameter-shifts (instead of  $\pm \frac{2\pi}{3}$  shifts in the present work), have outperformed Taylor approximation for  $L = 1, 2, 3, 4$ . Below, we will compare Algorithm 1 with gradient descent for  $L = 1$  and quantum analytic descent for  $L = 2$ . The technical reasons for this specific choice of comparisons will be explained in the respective sections.

### 2.5.1 Comparison with gradient descent

For functions  $f: \mathbb{R}^m \rightarrow \mathbb{R}$  of the form (1), gradient descent using the parameter-shift rules requires  $2m$  circuit evaluations per iteration. Keeping track of the value of  $f$  during the execution of gradient descent requires one additional circuit evaluation per iteration for a total of  $2m + 1$  evaluations, since computation of the gradient via the parameter-shift rules does not require knowledge of the value of  $f$  at the development point. With the choice of hyperparameter  $L = 1$ , Algorithm 1 requires  $2m + 1$  circuit evaluations per iteration by Theorem 3(i). Consequently, it makes sense to compare gradient descent to Algorithm 1 with  $L = 1$ , because in this case both algorithms require the same number of circuit evaluations per iteration.

A single iteration of both gradient descent and Algorithm 1 with  $L = 1$  corresponds to an optimization step with respect to an approximation that coincides with  $f$  up to first order around the development point. However, the approximations of  $f$  computed during the execution of Algorithm 1 are elements of the reproducing kernel Hilbert space  $H$  (and consequently trigonometric polynomials), whereas gradient descent corresponds to optimization steps with respect to linear approximations of  $f$ . Moreover, it follows from Theorem 3(ii) that the approximations of  $f$  computed during the execution of Algorithm 1 with  $L = 1$  coincide with  $f$  on the (affine) lines through the respective development point which are parallel to the coordinate axes of  $\mathbb{R}^m$ . Informally speaking, this means that if we move away from the development point along a single coordinate direction, the approximation is exact, i.e., it coincides with  $f$ . Consequently, there are, in general, regions in parameter space arbitrarily close to the development point where the approximation computed during execution of Algorithm 1 significantly outperforms the first order Taylor polynomial (which is the linear approximation relevant in the context of gradient descent). As mentioned above, in the experiments in [SEKR24b] the approximations featuring in Algorithm 1 with  $L = 1$ , albeit with  $\pm \frac{\pi}{2}$  parameter-shifts (instead of  $\pm \frac{2\pi}{3}$  shifts in the present work), have significantly outperformed first order Taylor approximation. In Section 3 of the present work we carry out extensive experiments where we do not only compare the quality of the local approximations, but also the performance of gradient descent and Algorithm 1 with  $L = 1$  when it comes to the actual goal of minimizing  $f$ .

### 2.5.2 Comparison with quantum analytic descent

Quantum analytic descent requires  $2m^2 + m + 1$  circuit evaluations per iteration. With the choice of hyperparameter  $L = 2$ , Algorithm 1 requires  $2m^2 + 1$  circuit evaluations per iteration by Theorem 3(i). So, Algorithm 1 with  $L = 2$  requires slightly fewer circuit evaluations than quantum analytic descent, but the number of circuit evaluations is the same asymptotically. Consequently, it makes sense to compare quantum analytic descent to Algorithm 1 with  $L = 2$ .

A single iteration of both quantum analytic descent and Algorithm 1 with  $L = 2$  corresponds to an optimization step with respect to an approximation that coincides with  $f$  up to second order around the development point. The approximations of  $f$  computed during execution of both algorithms are trigonometric polynomials that preserve the periodicity of  $f$ . Informally speaking, if we move away from the development point along *a single* coordinate direction, the approximation computed by quantum analytic descent is exact, i.e., it coincides with  $f$ . However, for the approximations computed during execution of Algorithm 1 with  $L = 2$  we have the following stronger guarantee (by Theorem 3(ii)): If we move away from the development point along *at most two* coordinate directions simultaneously, the approximation is exact, i.e., it coincides with  $f$ . In Section 3 of the present work we carry out extensive experiments where we do not only compare the quality of the local approximations, but also the performance of quantum analytic descent and Algorithm 1 with  $L = 2$  when it comes to the actual goal of minimizing  $f$ .

## 3 EXPERIMENTS

In this section, we present a detailed experimental comparison of kernel descent with  $L = 1$  versus gradient descent, as well as kernel descent with  $L = 2$  versus quantum analytic descent. As explained in Section 2.5, these pairings are chosen because of their roughly equivalent computational efforts in terms of circuit evaluations per iteration. The algorithms will be compared with respect to the quality of the local approximations (Section 3.2) and their performance in terms of their ability to minimize the objective function (Section 3.3). Before that, we describe the experimental setup in Section 3.1.

### 3.1 Experimental setup

In our experiments we neither take measurement shot noise nor quantum hardware noise into account. That is, all compared algorithms are provided with exact values of the objective function  $f$  computed via statevector simulation.

In order to ensure independence of our results from any particular choice of circuit or configuration, we repeatedly sample circuits, observables, and points in parameter space randomly in all our experiments. We proceed similarly to the experimental setup in [SEKR24a]: Points in parameter space are randomly sampled from the uniform distribution on  $[-\pi, \pi]^m$ . With the notation from Section 2.1, the observable  $\mathcal{M}$  is an  $n$ -qubit Pauli randomly sampled from the uniform distribution on  $\{I, X, Y, Z\}^{\otimes n} \setminus \{I^{\otimes n}\}$ . The generators  $G_1, \dots, G_m$  of the parametrized gates  $R_1, \dots, R_m$

are sampled (independently) from the uniform distribution on  $\{I, X, Y, Z\}^{\otimes n} \setminus \{I^{\otimes n}\}$ , and the  $n$ -qubit unitaries  $C_1, \dots, C_{m+1}$  are randomly sampled (independently) via the same procedure by which the individual layers in the well-known quantum volume test [CBS<sup>+</sup>19] are sampled. For a visual representation of the entire circuit we refer to Figure 1, the specific choice of the unitaries  $C_j$  is explained and visualized in Figure 2.

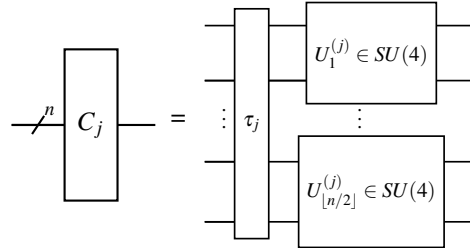


Figure 2: This figure shows the specific choice of unitaries  $C_j$  featuring in the experiments in Section 3: First, a permutation  $\tau_j \in \mathcal{S}_n$  is sampled uniformly at random. Subsequently, unitaries  $U_1^{(j)}, \dots, U_{[n/2]}^{(j)}$  are sampled independently from the Haar measure on  $SU(4)$ . These are then applied to the qubit pairs  $(\tau_j(1), \tau_j(2)), \dots, (\tau_j(2\lfloor n/2 \rfloor - 1), \tau_j(2\lfloor n/2 \rfloor))$  respectively. Note that this is precisely how the individual layers in the quantum volume test [CBS<sup>+</sup>19] are sampled.

### 3.2 Quality of the local approximations

Let  $p \in \mathbb{R}^m$  be a point in parameter space, let  $g: \mathbb{R}^m \rightarrow \mathbb{R}$  be a local approximation of  $f$  about  $p$ . In this subsection we will provide comparisons of the two algorithm pairs kernel descent with  $L = 1$  versus gradient descent and kernel descent with  $L = 2$  versus quantum analytic descent with respect to three notions of *error* at a point  $\theta \in \mathbb{R}^m$  that is “sufficiently close” to the development point  $p$ :

- The *value approximation error*

$$|f(\theta) - g(\theta)|,$$

which is the absolute value of the difference between the value of the true function and that of the local approximation.

- The *gradient approximation error in Euclidean norm*

$$\|\nabla f(\theta) - \nabla g(\theta)\|,$$

which is the Euclidean norm of the difference between the gradient of the true function and that of the local approximation (recall that this is relevant, since all compared algorithms – either explicitly or implicitly – apply gradient descent to the respective local approximations in an inner minimization loop).

- The *gradient approximation error in cosine distance*. That is, the cosine distance between the gradient of the true function and that of the local approximation

$$1 - \frac{\nabla f(\theta) \bullet \nabla g(\theta)}{\|\nabla f(\theta)\| \|\nabla g(\theta)\|},$$

where  $\bullet$  denotes the Euclidean dot product. The cosine distance allows us to only compare the error in the *direction* of the gradient of the approximation, ignoring the error in the *length*. This is of particular relevance for the experiments in Section 3.3.1.<sup>1</sup>

These three measures lead to six sets of comparisons (three comparisons per one of the two algorithm pairs), which will each be visualized via two kinds of scatter plots that highlight different aspects of the comparison. Since the process of sampling, error computation, plotting is the same for all six experiments, we will describe the procedure once for the first experiment, kernel descent with  $L = 1$  versus gradient descent with respect to the value approximation error. The others work analogously, just replace  $L = 1$  with  $L = 2$  and gradient descent with quantum analytic descent, and/or exchange the value approximation error for any of the other two error measures. The results of the experiments are described in Section 3.2.1.

**Sampling.** We denote the value approximation error at  $\theta$  by  $\mathcal{E}_\theta(f, g)$ . Now fix  $n = m = 10$  and repeat the following  $N = 25,000$  times:

1. A circuit, a point  $p \in \mathbb{R}^m$  and an observable  $\mathcal{M}$  are sampled randomly as explained in Section 3.1, and  $f$  is defined as in Section 2.1.
2. Determine the local approximations  $f_{\text{GD}}$  and  $f_{\text{KD}}$  to  $f$  about  $p$  computed by gradient descent and kernel descent with  $L = 1$ , respectively.
3. Randomly sample a point  $\theta$  in the vicinity of  $p$ ; specifically, we set  $\theta = p + \vartheta$ , where  $\vartheta$  is sampled from the uniform distribution on  $[-0.5, 0.5]^m$ .
4. Compute the distance  $d_\theta := \|\theta - p\| = \|\vartheta\|$  to the development point  $p$ .
5. Compute the errors  $\mathcal{E}_\theta(f, f_{\text{GD}})$  and  $\mathcal{E}_\theta(f, f_{\text{KD}})$ .

This process yields 25,000 data points of the form  $[d_\theta, \mathcal{E}_\theta(f, f_{\text{GD}}), \mathcal{E}_\theta(f, f_{\text{KD}})]$  which we use to create the two aforementioned types of scatter plots.

**The first type of scatter plot.** The goal of the first type of scatter plot is to directly compare the errors made by gradient descent and kernel descent. To this end, we plot the  $N = 25,000$  points of the form  $[\mathcal{E}_\theta(f, f_{\text{GD}}), \mathcal{E}_\theta(f, f_{\text{KD}})]$  in a two-dimensional coordinate system. The  $x$ -coordinate represents the error made by gradient descent, while the  $y$ -coordinate represents the error made by kernel descent with  $L = 1$ . As a consequence, points above the diagonal correspond to outcomes where gradient descent outperforms kernel descent, while points below the diagonal indicate the opposite.

Points on or above the diagonal are marked in blue, and points below the diagonal are marked in red. Our measure of success for kernel descent is the percentage of points that lie below the diagonal. However, this does not quantify the

margin by which one algorithm typically outperforms the other. To provide an indication of this margin, we plot a line through the origin, with its polar angle being the average of the polar angles of the  $N = 25,000$  plotted points.

**The second type of scatter plot.** The second type of scatter plot focuses on illustrating the dependence of the approximation errors on the distance to the development point  $p$ , which is not represented in the first type of plot. From each of the  $N = 25,000$  data points  $[d_\theta, \mathcal{E}_\theta(f, f_{\text{GD}}), \mathcal{E}_\theta(f, f_{\text{KD}})]$ , we derive two points:  $[d_\theta, \mathcal{E}_\theta(f, f_{\text{GD}})]$  and  $[d_\theta, \mathcal{E}_\theta(f, f_{\text{KD}})]$  and plot them in a two-dimensional coordinate system, marked in blue and red, respectively. This results in a scatter plot of  $2N = 50,000$  points.

Generally speaking, the closer a point is to the  $x$ -axis, the better the approximation performance of the corresponding algorithm. As a visual aid, we fit a curve of the form  $x \mapsto c \cdot x^2$  to each point cloud (minimizing the mean squared error), where  $c$  is the parameter being fit. We chose the exponent 2, since the local value approximation error of both algorithms is  $O(\|\theta - p\|^2)$ , see Theorem 3(iii).

For the five remaining combinations of algorithm pair and error notion, the exponent is likewise chosen according to the estimates in Theorem 3(iii). As a result of this construction, the curve that lies below the other indicates that the corresponding algorithm performs better in terms of approximation quality.

### 3.2.1 Results

Based on the criteria described above, kernel descent outperformed in all twelve scatter plots.

In the six scatter plots of the first type (see Figure 3), kernel descent won all comparisons, with at least 58% of the points—and often significantly more—marked in red in each plot.

In the six scatter plots of the second type (see Figure 4), kernel descent won all comparisons, as the red curve lies below the blue curve in every plot.

## 3.3 Performance of the algorithms

Here we compare the algorithms with respect to their ability to minimize the objective function. The comparisons of kernel descent with  $L = 1$  versus gradient descent and kernel descent with  $L = 2$  versus quantum analytic descent follow a similar pattern, albeit with some key differences which are imposed by the higher computational demands per iteration of the second pair of algorithms.

### 3.3.1 Kernel descent versus gradient descent

To level the playing field, we carry out kernel descent with  $L = 1$  and gradient descent in their most basic form without specialized enhancements such as learning rate adaptation. In particular, we assume that gradient descent operates with a fixed learning rate  $\alpha > 0$ . Moreover, we rescale the steps of the inner optimization loop of kernel descent so that their

<sup>1</sup>In order to prevent numerical instability and division by 0 in our experiments, a small positive constant was added to both factors appearing in the denominator.

combined length equals that of the corresponding gradient descent step. We will now describe the experiments in detail and then conclude with our observations.

**Circuit sampling and running the algorithms.** In order to keep the computational load manageable, we set  $n = m = 8$  and choose  $T = 20$  iterations per algorithm. We will compare the algorithms using  $N = 5,000$  randomly sampled circuits, and for each circuit we will test three different learning rates  $\alpha_1 = 7.0$ ,  $\alpha_2 = 8.5$  and  $\alpha_3 = 10.0$ . Each of the  $N = 5,000$  test runs will follow the scheme outlined below.

1. **Circuit sampling:** A circuit, an initial point  $\theta_0 \in \mathbb{R}^m$  and an observable  $\mathcal{M}$  are sampled randomly as explained in Section 3.1, and  $f$  is defined as in Section 2.1.
2. **Gradient descent runs:** Starting from initial point  $\theta_0$ , gradient descent with  $T = 20$  steps is executed three times with the three different learning rates:  $\alpha_1, \alpha_2$  and  $\alpha_3$ . This yields three sequences of points in parameter space which we denote by
 
$$\Theta_i^{\text{GD}} := \Theta^{(\text{GD}, \alpha_i)} := (\theta_0, \theta_1^{(\text{GD}, \alpha_i)}, \dots, \theta_{20}^{(\text{GD}, \alpha_i)}),$$
 where  $i = 1, 2, 3$ .
3. **Kernel descent runs:** Starting from initial point  $\theta_0$ , kernel descent with  $L = 1$  and  $T = 20$  steps is executed three times:
  - Denote the current point in parameter space after  $t$  iterations of kernel descent by  $\theta_t$ , and the local approximation of  $f$  around  $\theta_t$  by  $\tilde{f}_t$ . In the inner optimization loop we execute  $k = 100$  gradient descent steps with respect to  $\tilde{f}_t$ .
  - In the three executions of kernel descent, the learning rates for the inner optimization loops are  $\alpha_1/k = 0.07$ ,  $\alpha_2/k = 0.085$  and  $\alpha_3/k = 0.1$ . This rescaling of the learning rates accounts for the number of gradient descent steps taken in the inner loop.
  - At each of the  $k$  gradient descent steps of the inner optimization loop starting at  $\theta_t$ , the gradient of the local approximation  $\tilde{f}_t$  is rescaled to have length  $\|\nabla f(\theta_t)\|$  (numerical instability and division by 0 are prevented by adding a small positive constant to the occurring denominators). Since  $\nabla f(\theta_t) = \nabla \tilde{f}_t(\theta_t)$  by Theorem 3(iii), computation of  $\nabla f(\theta_t)$  does not require any additional circuit evaluations.

We thus obtain three sequences of points in parameter space, one per learning rate, which we denote by

$$\Theta_i^{\text{KD}} := \Theta^{(\text{KD}, \alpha_i)} := (\theta_0, \theta_1^{(\text{KD}, \alpha_i)}, \dots, \theta_{20}^{(\text{KD}, \alpha_i)}),$$

where  $i = 1, 2, 3$ .

The final outcome of this procedure is a family

$$\Theta := (\Theta_i^A)_{A \in \{\text{GD}, \text{KD}\}, i \in \{1, 2, 3\}}$$

of six point sequences in parameter space—one per combination of algorithm and learning rate—for each of the  $N = 5,000$  randomly sampled circuits.

**Normalization.** Since the circuit, initial point, and observable were sampled randomly in each of the  $N = 5,000$  test runs, we cannot directly compare the values of the objective function  $f$  between different runs. We remedy this by normalizing the  $f$ -values of the point sequences we computed. Specifically, for each of the  $N = 5,000$  families  $\Theta$ , the following is carried out: Let  $v$  be the minimal value of  $f$  attained at a point in any of the sequences in  $\Theta$ . That is,  $v = \min(\{f(\theta_0), f(\theta_t^{(\text{GD}, \alpha_i)}), f(\theta_t^{(\text{KD}, \alpha_i)}) \mid t \in \{1, \dots, 20\}, i \in \{1, 2, 3\}\})$ .<sup>2</sup>

Now let

$$\ell: \mathbb{R} \rightarrow \mathbb{R}, x \mapsto \frac{x-v}{f(\theta_0)-v} \quad (3)$$

be the uniquely determined affine linear map that maps  $f(\theta_0)$  to 1 and  $v$  to 0. Applying  $\ell$  component-wise to the sequences of  $f$ -values corresponding to the point sequences in  $\Theta$ , we obtain three normalized sequences for gradient descent,

$$\tilde{f}_i^{\text{GD}} := (1, \ell(f(\theta_1^{(\text{GD}, \alpha_i)})), \dots, \ell(f(\theta_{20}^{(\text{GD}, \alpha_i)}))),$$

and three normalized sequences for kernel descent,

$$\tilde{f}_i^{\text{KD}} := (1, \ell(f(\theta_1^{(\text{KD}, \alpha_i)})), \dots, \ell(f(\theta_{20}^{(\text{KD}, \alpha_i)}))),$$

where  $i = 1, 2, 3$ .

**Illustration and observations.** For a fixed learning rate  $\alpha_i$ , where  $i \in \{1, 2, 3\}$ , and a fixed algorithm  $A \in \{\text{GD}, \text{KD}\}$  we can obtain an averaged sequence of normalized  $f$ -values by taking the component-wise average over all  $N = 5,000$  normalized sequences  $\tilde{f}_i^A$ . The so-obtained sequence can be interpreted as the average performance of the considered combination of algorithm and learning rate. Comparisons of these average performances are visualized in Figure 5.

Upon closer inspection we realized that, for the smallest learning rate  $\alpha_1$ , the direction of the *true* gradient vector did typically not change by much between two consecutive gradient descent steps. Because of this, and since we ensured that the length of the path in parameter space traversed during the inner optimization loop of kernel descent equals the length of the corresponding gradient descent step, one cannot expect kernel descent with  $L = 1$  to significantly outperform gradient descent at learning rate  $\alpha_1$  in our experiments. Nevertheless, as the quality of the local approximations computed by kernel descent with  $L = 1$  is typically higher than the quality of the best linear approximation (see Section 3.2), kernel descent with  $L = 1$  can still be expected to perform slightly better than gradient descent, even at small learning rates. These expectations are confirmed in Figure 5a.

<sup>2</sup>In the pathological case where  $v$  is not smaller than  $f(\theta_0)$ , one would discard the family  $\Theta$  and compute another one. However, this did not happen in our experiments.

For the largest learning rate,  $\alpha_3$ , the steps taken by gradient descent were often too large and the algorithm did not converge. Contrary to this, in the inner optimization loop of the corresponding execution of kernel descent with  $L = 1$ , the descent often got caught in a local minimum of the local approximation, which effectively prevented the algorithm from moving away too far from the development point. As a result, kernel descent typically converged, while gradient descent typically did not. This is mirrored in Figure 5c.

For learning rate  $\alpha_2$ , we observed a mixture of the phenomena which we observed for learning rates  $\alpha_1$  and  $\alpha_3$ . Non-surprisingly, the robustness advantages of kernel descent (against taking exceedingly large steps in parameter space) were less pronounced than with learning rate  $\alpha_3$ , while the advantages in terms of speed of descent (owing to the better approximation quality, see Section 3.2) were more pronounced than with learning rate  $\alpha_1$ . The results for learning rate  $\alpha_2$  are visualized in Figure 5b.

Out of all six combinations of algorithm and learning rate, kernel descent with  $L = 1$  and learning rate  $\alpha_3$  performed the best in our experiments. Moreover, every combination involving kernel descent performed better than all combinations involving gradient descent, see Figures 5d, 5e, 5f.

In conclusion, kernel descent with  $L = 1$  outperformed gradient descent at small learning rates in our experiments, which we ascribe to the higher quality of the local approximations, see Section 3.2. Moreover, kernel descent with  $L = 1$  was more robust with respect to the choice of learning rate, which we ascribe to the presence of local minima for the local approximations computed during kernel descent with  $L = 1$ . While the local approximations computed during kernel descent necessarily have local (and global) minima, it is not clear whether the robustness effect we observed in our experiments will continue to hold outside of our experimental setup. An investigation of the latter is left for future work.

### 3.3.2 Kernel descent versus quantum analytic descent

The comparison of kernel descent with  $L = 2$  versus quantum analytic descent follows a similar scheme as the comparison of kernel descent with  $L = 1$  versus gradient descent. Key differences concern the random sampling of the observable and the stopping criteria for the inner optimization loops of the algorithms.

**Circuit sampling.** The circuit and the initial point in parameter space are sampled precisely as described in Section 3.1. The observable  $\mathcal{M}$  is sampled as follows: We randomly sample (independently) twenty  $n$ -qubit Paulis  $\mathcal{P}_1, \dots, \mathcal{P}_{20}$  from the uniform distribution on  $\{I, X, Y, Z\}^{\otimes n}$ ; we also randomly sample (independently) coefficients  $c_1, \dots, c_{20}$  from the standard normal distribution. We then set  $\mathcal{M} := \sum_{i=1}^{20} c_i \mathcal{P}_i$ .

**The inner optimization loop.** To ensure a fair comparison, the inner optimization loop was conducted in the same way for kernel descent and quantum analytic descent; specifically, we used gradient descent with learning rate

0.01 and applied the same stopping criterion to both algorithms. In order to be as impartial as possible, we used one of the stopping criteria given in the original work on quantum analytic descent [KB22]:

The inner optimization loop is stopped as soon as the *true* value of  $f$  is increased. Since every determination of the true value of  $f$  requires an additional circuit evaluation, we only determine the true value of  $f$  every 1000<sup>th</sup> step of the inner loop. Moreover, in order to prevent an infinite loop and to upper-bound the number of circuit evaluations per iteration of the algorithms, we set an upper bound of 10000 steps after which the inner optimization loop is aborted, even if the true value of  $f$  has not been found to increase. Consequently, at most 9 additional circuit evaluations are incurred as a result of the inner optimization loop – which is negligible in comparison to the overall number of circuit evaluations per iteration.

**Experiment execution.** Due to the aforementioned higher computational cost per iteration the number of test runs for the current comparison is reduced from  $N = 5,000$  to  $N = 500$ . In each run the following is performed:

1. A circuit, an initial point  $\theta_0 \in \mathbb{R}^m$  and an observable  $\mathcal{M}$  are sampled randomly as explained previously.
2. Starting from initial point  $\theta_0$ , both quantum analytic descent and kernel descent with  $L = 2$  are executed each with  $T = 5$  steps (with inner optimization loop as described above). We denote the resulting sequences of points in parameter space by

$$\Theta^{\text{QAD}} := \left( \theta_0, \theta_1^{(\text{QAD})}, \dots, \theta_5^{(\text{QAD})} \right)$$

and

$$\Theta^{\text{KD}} := \left( \theta_0, \theta_1^{(\text{KD})}, \dots, \theta_5^{(\text{KD})} \right),$$

respectively.

**Normalization.** As in Section 3.3.1 we need to introduce a normalization step before we can compare the values of the objective function  $f$  between different runs. For each of the  $N = 500$  runs we proceed as follows: We denote the minimal value of  $f$  attained during execution of the two algorithms by  $v$ . That is,

$$v = \min(\{f(\theta_0), f(\theta_t^{(\text{QAD})}), f(\theta_t^{(\text{KD})}) \mid t \in \{1, \dots, 5\}\}).$$

As above, no pathological cases (where  $v = f(\theta_0)$ ) arose and thus no exception handling was necessary.

Using  $v$ , we define  $\ell : \mathbb{R} \rightarrow \mathbb{R}$  as in (3). Applying  $\ell$  component-wise to the sequences of values obtained during execution of the algorithms, we obtain normalized sequences

$$\bar{f}^{\text{QAD}} := \left( 1, \ell(f(\theta_1^{(\text{QAD})})), \dots, \ell(f(\theta_5^{(\text{QAD})})) \right),$$

and

$$\bar{f}^{\text{KD}} := \left( 1, \ell(f(\theta_1^{(\text{KD})})), \dots, \ell(f(\theta_5^{(\text{KD})})) \right).$$

As in Section 3.3.1, we then compute the component-wise average of the  $N = 500$  normalized sequences  $\bar{f}^{\text{QAD}}$  (resp.  $\bar{f}^{\text{KD}}$ ).



**Results.** Kernel descent with  $L = 2$  clearly outperformed quantum analytic descent, in the sense that the average curve for kernel descent runs below that of quantum analytic descent, see Figure 6.

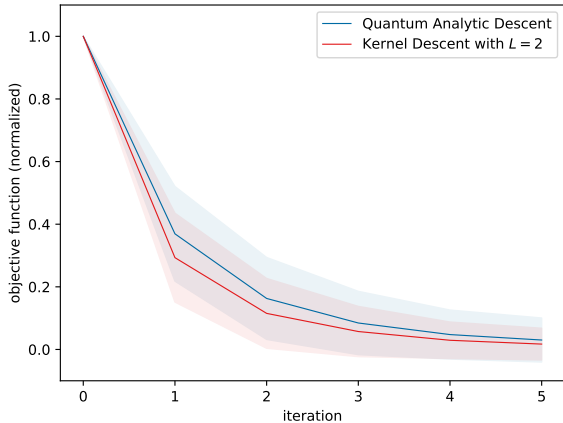


Figure 6: This figure shows the performance of quantum analytic descent and kernel descent with  $L = 2$  averaged over  $N = 500$  respective executions. In each execution, the circuit, observable and initial point in parameter space were sampled randomly. Consequently, for the sake of comparability, we introduced a normalization step before averaging; see Section 3.3.2 for details. We also indicate the respective standard deviations.

## 4 CONCLUSION

In this article we introduced kernel descent (KD), a novel algorithm for minimizing the functions underlying variational quantum algorithms. More precisely, KD is an algorithm for finding a choice of parameters for a parametrized quantum circuit that minimizes the expected value of a given observable with respect to the state computed by this circuit.

As is the case for quantum analytic descent, each iteration of our algorithm involves using a quantum device to construct a classical local approximation to the objective function and subsequently carrying out a classical optimization routine in order to minimize this approximation. The local approximations are constructed by exploiting the fact that the functions computed by variational quantum algorithms are contained in a set which naturally carries the structure of a reproducing kernel Hilbert space.

This added structure also serves as a heuristic explanation for the fact that the local approximations constructed during execution of our algorithm significantly outperform  $L$ -th order Taylor approximation in our experiments despite not requiring a larger number of quantum circuit evaluations to compute. Here,  $L$  is a hyperparameter which controls the order of the local approximations featuring in our algorithm. After theoretically comparing our algorithm to gradient descent and to quantum analytic descent, we carried out extensive experiments to demonstrate the validity of our approach.

Potential topics for future research include, but are not limited to, the following:

- In the present work we considered parametrized gates of the form  $x \mapsto \exp(-i\frac{x}{2}G)$  whose Hermitian generators  $G$  were assumed to have as set of eigenvalues  $\{-1, 1\}$ . While this includes the often-studied case where  $G$  is a (non-identity) tensor product of Pauli matrices, this still limits the generality of our approach. In light of this, a natural direction for future work would be to extend our results by imposing less restrictive assumptions on the eigenvalues of the generators of the occurring parametrized gates.
- While we have demonstrated the capabilities of our local approximations both experimentally and with heuristic arguments, it would be desirable to prove rigorous error estimates. While it is straight-forward to show that the approximation error satisfies

$$|f(p + \vartheta) - \tilde{f}(p + \vartheta)| = O(\|\vartheta\|^{L+1}),$$

this does not explain why our local approximations outperform  $L$ -th order Taylor approximation in our experiments. However, we know that the approximation is exact if  $\vartheta$  is contained in a subspace of  $\mathbb{R}^m$  that is spanned by at most  $L$  of the coordinate axes. In light of this, it would be natural to attempt to derive error estimates in terms of the distance of  $\vartheta$  to the union of these subspaces. Moreover, while less meaningful in the context of estimating the *local* approximation error, it would be interesting to further exploit the reproducing kernel Hilbert space structure of  $H$  in order to obtain error estimates in terms of the  $L^2$ -norm.

- Our theoretical considerations in Section 2 take neither measurement shot noise nor quantum hardware noise into account. A natural next step would be to thoroughly analyse – both theoretically and experimentally – how our algorithm performs in the presence of noise. In particular, it would be useful to develop an (adaptive) measurement shot allocation strategy as in [KB22], [Ito23] and [TY22].

## ACKNOWLEDGEMENT

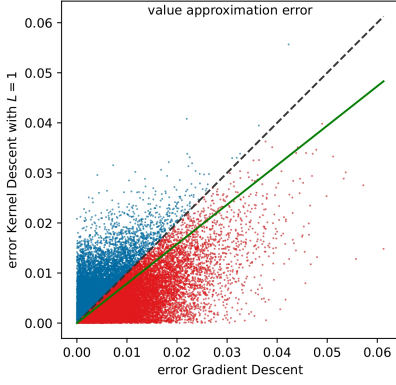
This article was written as part of the Qu-Gov project, which was commissioned by the German Federal Ministry of Finance. The authors want to extend their gratitude to Kim Nguyen, Manfred Paeschke, Oliver Muth, Andreas Wilke, and Yvonne Ripke for their continuous encouragement and support.

## References

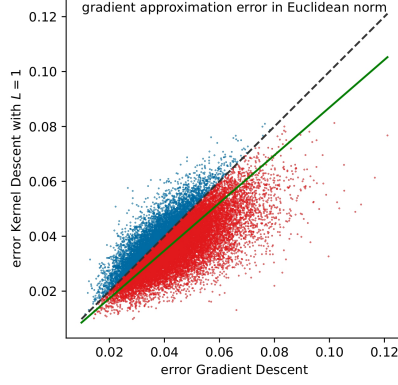
- [AKH<sup>+</sup>23] Amira Abbas, Robbie King, Hsin-Yuan Huang, William J. Huggins, Ramis Movassagh, Dar Gilboa, and Jarrod Ryan McClean. On quantum backpropagation, information reuse, and cheating measurement collapse. In *Thirty-seventh Conference on Neural Information Processing Systems*, 2023. URL: <https://openreview.net/forum?>

- id=HF6bnhfSqH, arXiv:2305.13362, doi:10.48550/arXiv.2305.13362.
- [Ama98] Shun-ichi Amari. Natural Gradient Works Efficiently in Learning. *Neural Computation*, 10(2):251–276, February 1998. doi:10.1162/089976698300017746.
- [BWP23] Joseph Bowles, David Wierichs, and Chae-Yeun Park. Backpropagation scaling in parameterised quantum circuits, 2023. arXiv:2306.14962, doi:10.48550/arXiv.2306.14962.
- [CAB<sup>+</sup>21] M. Cerezo, Andrew Arrasmith, Ryan Babbush, Simon C. Benjamin, Suguru Endo, Keisuke Fujii, Jarrod R. McClean, Kosuke Mitarai, Xiao Yuan, Lukasz Cincio, and Patrick J. Coles. Variational quantum algorithms. *Nature Reviews Physics*, 3(9):625–644, August 2021. URL: <http://dx.doi.org/10.1038/s42254-021-00348-9>, doi:10.1038/s42254-021-00348-9.
- [CBS<sup>+</sup>19] Andrew W. Cross, Lev S. Bishop, Sarah Sheldon, Paul D. Nation, and Jay M. Gambetta. Validating quantum computers using randomized model circuits. *Phys. Rev. A*, 100:032328, Sep 2019. URL: <https://link.aps.org/doi/10.1103/PhysRevA.100.032328>, arXiv:1811.12926, doi:10.1103/PhysRevA.100.032328.
- [HLSS15] Elad Hazan, Kfir Yehuda Levy, and Shai Shalev-Shwartz. Beyond convexity: Stochastic quasi-convex optimization. In *Neural Information Processing Systems*, 2015.
- [Ito23] Kosuke Ito. Latency-aware adaptive shot allocation for run-time efficient variational quantum algorithms, 2023. URL: <https://arxiv.org/abs/2302.04422>, arXiv:2302.04422.
- [KB15] Diederik Kingma and Jimmy Ba. Adam: A method for stochastic optimization. In *International Conference on Learning Representations (ICLR)*, San Diego, CA, USA, 2015.
- [KB22] Bálint Koczor and Simon C. Benjamin. Quantum analytic descent. *Phys. Rev. Res.*, 4:023017, April 2022. arXiv:2008.13774, doi:10.1103/PhysRevResearch.4.023017.
- [MBK21] Andrea Mari, Thomas R. Bromley, and Nathan Killoran. Estimating the gradient and higher-order derivatives on quantum hardware. *Physical Review A*, 103(1), January 2021. arXiv:2008.06517, doi:10.1103/physreva.103.012405.
- [MNKF18] Kosuke Mitarai, Makoto Negoro, Masahiro Kitagawa, and Keisuke Fujii. Quantum circuit learning. *Physical Review A*, 98(3), September 2018. arXiv:1803.00745, doi:10.1103/physreva.98.032309.
- [Nes83] Yurii Nesterov. A method for unconstrained convex minimization problem with the rate of convergence  $o(1/k^2)$ . *Doklady AN USSR*, 269:543–547, 1983.
- [NFT20] Ken M. Nakanishi, Keisuke Fujii, and Syngae Todo. Sequential minimal optimization for quantum-classical hybrid algorithms. *Phys. Rev. Res.*, 2:043158, October 2020. URL: <https://link.aps.org/doi/10.1103/PhysRevResearch.2.043158>, doi:10.1103/PhysRevResearch.2.043158.
- [NM65] John A. Nelder and Roger Mead. A Simplex Method for Function Minimization. *The Computer Journal*, 7(4), January 1965. doi:10.1093/comjnl/7.4.308.
- [OGB21] Mateusz Ostaszewski, Edward Grant, and Marcello Benedetti. Structure optimization for parameterized quantum circuits. *Quantum*, 5:391, January 2021. arXiv:1905.09692, doi:10.22331/q-2021-01-28-391.
- [PIOM19] Robert M. Parrish, Joseph T. Iosue, Asier Ozaeta, and Peter L. McMahon. A jacobi diagonalization and anderson acceleration algorithm for variational quantum algorithm parameter optimization, 2019. URL: <https://arxiv.org/abs/1904.03206>, arXiv:1904.03206.
- [Pow64] Michael J. D. Powell. An efficient method for finding the minimum of a function of several variables without calculating derivatives. *The Computer Journal*, 7(2), January 1964. doi:10.1093/comjnl/7.2.155.
- [Pow94] Michael J. D. Powell. *A Direct Search Optimization Method That Models the Objective and Constraint Functions by Linear Interpolation*, pages 51–67. Springer Netherlands, 1994. doi:10.1007/978-94-015-8330-5\_4.
- [SBG<sup>+</sup>19] Maria Schuld, Ville Bergholm, Christian Gogolin, Josh Izaac, and Nathan Killoran. Evaluating analytic gradients on quantum hardware. *Physical Review A*, 99(3), March 2019. arXiv:1811.11184, doi:10.1103/physreva.99.032331.
- [SEKR24a] Lars Simon, Holger Eble, Hagen-Henrik Kowalski, and Manuel Radons. Denoising Gradient Descent in Variational Quantum Algorithms, 2024. arXiv:2403.03826, doi:10.48550/arXiv.2403.03826.

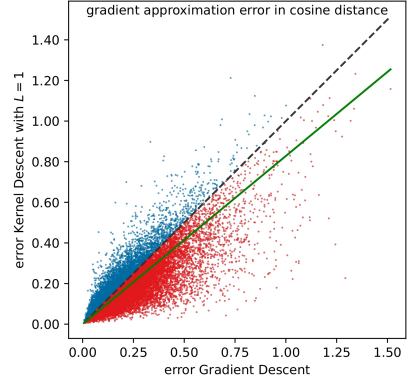
- [SEKR24b] Lars Simon, Holger Eble, Hagen-Henrik Kowalski, and Manuel Radons. Interpolating parametrized quantum circuits using blackbox queries. *SIAM Journal on Scientific Computing (accepted)*, 2024. arXiv:2310.04396, doi:10.48550/arXiv.2310.04396.
- [SIKC20] James Stokes, Josh Izaac, Nathan Killoran, and Giuseppe Carleo. Quantum Natural Gradient. *Quantum*, 4:269, May 2020. doi:10.22331/q-2020-05-25-269.
- [SR23a] Lars Simon and Manuel Radons. Algorithms for the Training of Neural Support Vector Machines, 2023. arXiv:2308.07204.
- [SR23b] Lars Simon and Manuel Radons. On Neural Quantum Support Vector Machines. *Quantum Machine Intelligence*, 6(3), 2023. arXiv:2308.08467.
- [SSM21] Maria Schuld, Ryan Sweke, and Johannes Jakob Meyer. Effect of data encoding on the expressive power of variational quantum-machine-learning models. *Physical Review A*, 103(3), March 2021. arXiv:2008.08605, doi:10.1103/physreva.103.032430.
- [SYRY21] Y. Suzuki, H. Yano, R. Raymond, and N. Yamamoto. Normalized gradient descent for variational quantum algorithms. In *2021 IEEE International Conference on Quantum Computing and Engineering (QCE)*, pages 1–9, Los Alamitos, CA, USA, October 2021. IEEE Computer Society. doi:10.1109/QCE52317.2021.00015.
- [TY22] Shiro Tamiya and Hayata Yamasaki. Stochastic gradient line bayesian optimization for efficient noise-robust optimization of parameterized quantum circuits. *npj Quantum Information*, 8(1):90, July 2022. doi:10.1038/s41534-022-00592-6.
- [VT18] Javier Gil Vidal and Dirk Oliver Theis. Calculus on parameterized quantum circuits, 2018. URL: <https://arxiv.org/abs/1812.06323>, arXiv:1812.06323.
- [WIWL22] David Wierichs, Josh Izaac, Cody Wang, and Cedric Yen-Yu Lin. General parameter-shift rules for quantum gradients. *Quantum*, 6:677, March 2022. arXiv:2107.12390, doi:10.22331/q-2022-03-30-677.



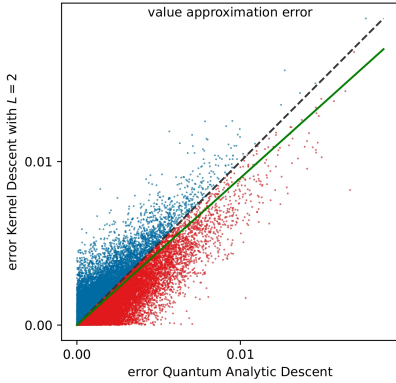
(a) Comparison between gradient descent and kernel descent with  $L = 1$  wrt. value approximation error. Kernel descent outperformed gradient descent in 63.7% of the outcomes.



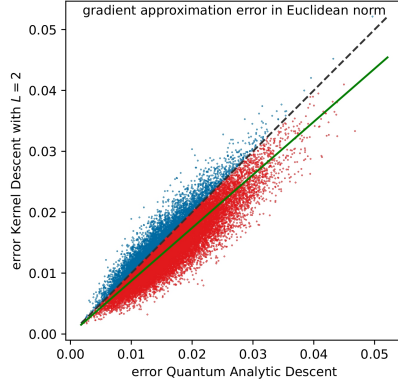
(b) Comparison between gradient descent and kernel descent with  $L = 1$  wrt. gradient approximation error in Euclidean norm. Kernel descent outperformed gradient descent in 76.2% of the outcomes.



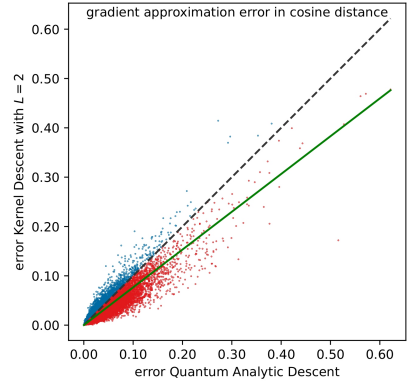
(c) Comparison between gradient descent and kernel descent with  $L = 1$  wrt. gradient approximation error in cosine distance. Kernel descent outperformed gradient descent in 71.3% of the outcomes.



(d) Comparison between quantum analytic descent and kernel descent with  $L = 2$  wrt. value approximation error. Kernel descent outperformed quantum analytic descent in 58.7% of the outcomes.

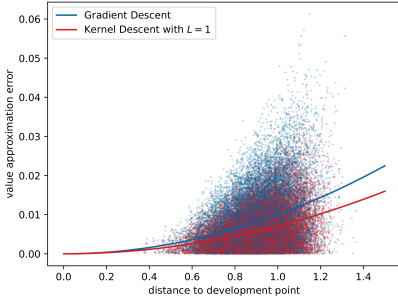


(e) Comparison between quantum analytic descent and kernel descent with  $L = 2$  wrt. gradient approximation error in Euclidean norm. Kernel descent outperformed quantum analytic descent in 79.9% of the outcomes.

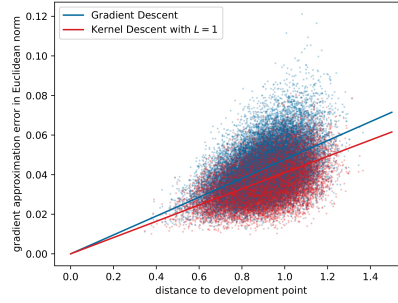


(f) Comparison between quantum analytic descent and kernel descent with  $L = 2$  wrt. gradient approximation error in cosine distance. Kernel descent outperformed quantum analytic descent in 78.5% of the outcomes.

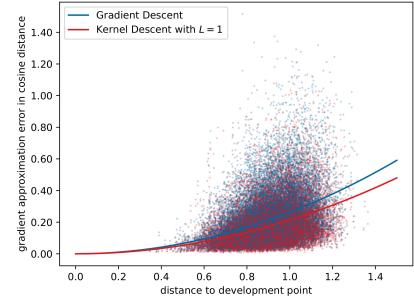
Figure 3: This figure shows the scatter plots of the first type from Section 3.2. Points below the diagonal (colored red) correspond to outcomes where kernel descent outperformed the algorithm it was being compared to. The green line is the line through the origin, whose polar angle is the average of the polar angles of the  $N = 25,000$  points appearing in the scatter plot. The fact that the green lines are running below the diagonals is a further indication that kernel descent outperformed the algorithm it was being compared to; see Section 3.2 for details.



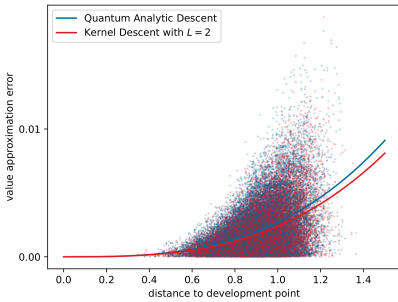
(a) Comparison between gradient descent and kernel descent with  $L = 1$  wrt. value approximation error. We fit curves of the form  $x \mapsto c \cdot x^2$  to both point clouds.



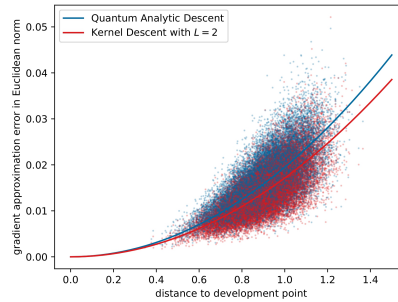
(b) Comparison between gradient descent and kernel descent with  $L = 1$  wrt. gradient approximation error in Euclidean norm. We fit curves of the form  $x \mapsto c \cdot x^1$  to both point clouds.



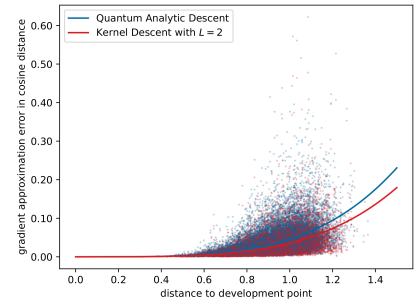
(c) Comparison between gradient descent and kernel descent with  $L = 1$  wrt. gradient approximation error in cosine distance. We fit curves of the form  $x \mapsto c \cdot x^2$  to both point clouds.



(d) Comparison between quantum analytic descent and kernel descent with  $L = 2$  wrt. value approximation error. We fit curves of the form  $x \mapsto c \cdot x^3$  to both point clouds.

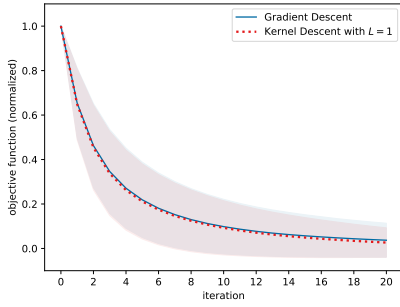


(e) Comparison between quantum analytic descent and kernel descent with  $L = 2$  wrt. gradient approximation error in Euclidean norm. We fit curves of the form  $x \mapsto c \cdot x^2$  to both point clouds.

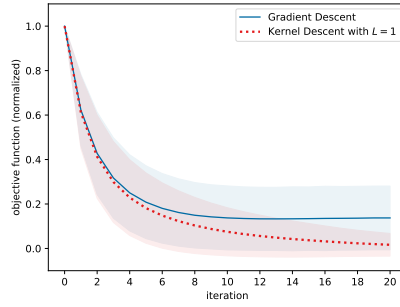


(f) Comparison between quantum analytic descent and kernel descent with  $L = 2$  wrt. gradient approximation error in cosine distance. We fit curves of the form  $x \mapsto c \cdot x^4$  to both point clouds.

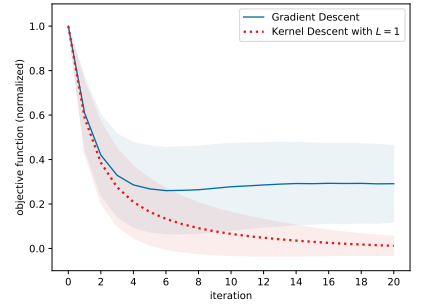
Figure 4: This figure shows the scatter plots of the second type from Section 3.2. The red curve running below the blue curve indicates that kernel descent outperformed the algorithm it was being compared to; see Section 3.2 for details.



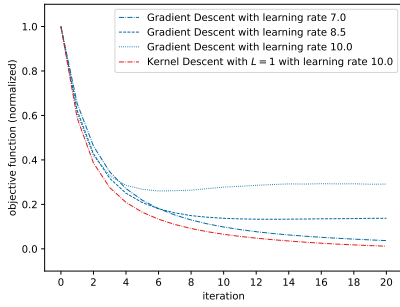
(a) Comparison at learning rate  $\alpha_1 = 7.0$ .



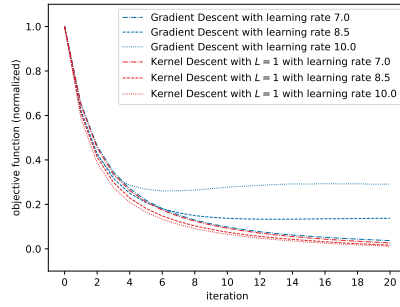
(b) Comparison at learning rate  $\alpha_2 = 8.5$ .



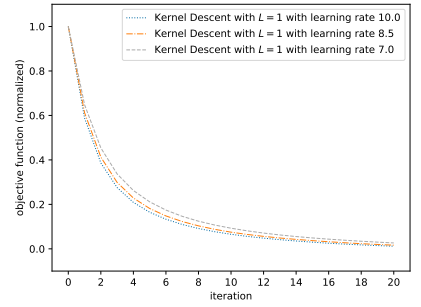
(c) Comparison at learning rate  $\alpha_3 = 10.0$ .



(d) Comparison between gradient descent at learning rates  $\alpha_1$ ,  $\alpha_2$ ,  $\alpha_3$  and kernel descent with  $L = 1$  at learning rate  $\alpha_3$ .



(e) Comparison between gradient descent and kernel descent with  $L = 1$  at learning rates  $\alpha_1$ ,  $\alpha_2$ ,  $\alpha_3$ .



(f) Comparison between learning rates  $\alpha_1$ ,  $\alpha_2$ ,  $\alpha_3$  for kernel descent with  $L = 1$ .

Figure 5: This figure shows the performance of gradient descent and kernel descent with  $L = 1$  for three different learning rates, averaged over  $N = 5,000$  respective executions. In each execution, the circuit, observable and initial point in parameter space were sampled randomly. Consequently, for the sake of comparability, we introduced a normalization step before averaging; see Section 3.3.1 for details. In Figures 5a, 5b, 5c we compare gradient descent to kernel descent with  $L = 1$  at learning rates  $\alpha_1 = 7.0$ ,  $\alpha_2 = 8.5$  and  $\alpha_3 = 10.0$  respectively; we also indicate the respective standard deviations. In Figures 5d, 5e, 5f we make comparisons between different learning rates.